Received: 7 April 2023 | Accepted: 13 August 2023

DOI: 10.1097/HEP.0000000000000591

ORIGINAL ARTICLE

OPEN

Spatial proteomics of immune microenvironment in nonalcoholic steatohepatitis-associated hepatocellular carcinoma

Meiyi Li[1] | Lina Wang[2,3] | Liang Cong[3] | Chi Chun Wong[1] | Xiang Zhang[1] | Huarong Chen[1] | Tao Zeng[4] | Bin Li[5] | Xian Jia[6] | Jihui Huo[3] | Yuhua Huang[7] | Xiaoxue Ren[3] | Sui Peng[3,5] | Guo Fu[6] | Lixia Xu[3,8] | Joseph J.Y. Sung[3,9] | Ming Kuang[2,3] | Xiaoxing Li[3] | Jun Yu[1,3]

[1]State Key Laboratory of Digestive Disease, Department of Medicine and Therapeutics, The Chinese University of Hong Kong, Hong Kong SAR, China

[2]Center of Hepato-Pancreato-Biliary Surgery, the First Affiliated Hospital, Sun Yat-sen University, Guangzhou, China

[3]Institute of Precision Medicine, the First Affiliated Hospital, Sun Yat-sen University, Guangzhou, China

[4]Guangzhou Laboratory, Guangzhou, China

[5]Clinical Trial Unit, The First Affiliated Hospital, Sun Yat-sen University, Guangzhou, China

[6]State Key Laboratory of Cellular Stress Biology, Innovation Center for Cell Signaling Network, School of Life Sciences, School of Medicine, Xiamen University, Xiamen, China

[7]State Key Laboratory of Oncology in South China, Department of Pathology, Collaborative Innovation Center for Cancer Medicine, Sun Yat-sen University Cancer Center, Guangzhou, Guangdong, China

[8]Department of Oncology, the First Affiliated Hospital, Sun Yat-sen University, Guangzhou, China

[9]Lee Kong Chian School of Medicine, Nanyang Technological University, Singapore

Correspondence
Jun Yu, Department of Medicine and Therapeutics, State Key Laboratory of Digestive Disease, The Chinese University of Hong Kong, Shatin, N.T., Hong Kong, 999077 China.
Email: junyu@cuhk.edu.hk

Xiaoxing Li, Institute of Precision Medicine, the First Affiliated Hospital, Sun Yat-sen University, Guangzhou, 510080, China.
Email: lixiaox23@mail.sysu.edu.cn

Abstract

Background and Aims: NASH-HCC is inherently resistant to immune checkpoint blockade, but its tumor immune microenvironment is largely unknown.

Approach and Results: We applied the imaging mass cytometry to construct a spatially resolved single-cell atlas from the formalin-fixed and paraffin-embedded tissue sections from patients with NASH-HCC, virus-HCC (HBV-HCC and HCV-HCC), and healthy donors. Based on 35 biomarkers, over 750,000 individual cells were categorized into 13 distinct cell types, together with the expression of key immune functional markers. Higher infiltration of T cells, myeloid-derived suppressor cell (MDSCs), and tumor-associated

Abbreviations: CPM, cell phenotype map; FFPE, formalin-fixed and paraffin-embedded; GZMB, granzyme B; H&E, hematoxylin and eosin; ICB, immune checkpoint blockade; ICOS, inducible T cell costimulator; ICP, immune checkpoint proteins; IMC, imaging mass cytometry; IRP, immunoregulatory protein; LDA, linear discriminant analysis; M, margin; MDSC, myeloid-derived suppressor cell; M-MDSC, monocytic myeloid-derived suppressor cell; MT, tumorous region near margin; NKT, natural killer T cell; NM, nontumorous; P, peritumor; PCC, Pearson correlation coefficient; PD-1, programmed cell death 1; PD-L1, programmed cell death-ligand 1; PMN-MDSC, polymorphonuclear myeloid-derived suppressor cell; ROI, region of interest; T, tumor; TAM, tumor-associated macrophage; TIME, tumor immune microenvironment; T_{reg}, regulatory T cell.

Meiyi Li, Lina Wang, Liang Cong, and Chi Chun Wong are co-first authors.

Supplemental Digital Content is available for this article. Direct URL citations are provided in the HTML and PDF versions of this article on the journal's website, www.hepjournal.com.

This is an open access article distributed under the terms of the Creative Commons Attribution-Non Commercial-No Derivatives License 4.0 (CCBY-NC-ND), where it is permissible to download and share the work provided it is properly cited. The work cannot be changed in any way or used commercially without permission from the journal.
Copyright © 2023 The Author(s). Published by Wolters Kluwer Health, Inc.

macrophages (TAMs) in HCC compared to controls. The distribution of immune cells in NASH-HCC is spatially heterogeneous, enriched at adjacent normal tissues and declined toward tumors. Cell-cell connections analysis revealed the interplay of MDSCs and TAMs with $CD8^+$ T cells in NASH-HCC. In particular, exhausted programmed cell death 1 ($PD\text{-}1^+$)$CD8^+$ T cells connected with programmed cell death-ligand 1 ($PD\text{-}L1^+$)/inducible T cell costimulator ($ICOS^+$) MDSCs and TAMs in NASH-HCC, but not in viral HCC. In contrast, $CD4^+$/$CD8^+$ T cells with granzyme B positivity were reduced in NASH-HCC. Tumor cells expressed low PD-L1 and showed few connections with immune cells.

Conclusions: Our work provides the first detailed spatial map of single-cell phenotypes and multicellular connections in NASH-HCC. We demonstrate that interactions between MDSCs and TAMs with effector T cells underlie immunosuppression in NASH-HCC and are an actionable target.

INTRODUCTION

HCC is a leading cause of cancer-related deaths globally. Conventionally, chronic liver infections associated with the HBV or HCV are major risk factors for HCC.[1] Nevertheless, NASH is an emergent cause of HCC,[2] especially in light of the rising incidence of NASH worldwide. NASH-HCC follows a distinct pathology, characterized by disease progression from simple steatosis, NASH, cirrhosis, and eventually HCC.[3] Hepatic necro-inflammation is driven by ectopic deposition of lipids such as triglycerides[4] and cholesterol,[5] with a very different tumor microenvironment compared to virus-associated HCC. As a consequence, NASH-HCC exhibits divergent therapeutic responses on immune checkpoint blockade (ICB) therapy.[6,7] While ICB therapy is now the mainstay treatment of virus-associated HCC with survival benefit over sorafenib,[8] in NASH-HCC the use of ICB therapy is paradoxically associated with detrimental effects and poor survival.[6,7] Hence, there is an unmet need to understand the unique tumor immune microenvironment (TIME) of NASH-HCC that renders ICB nonresponse compared to virus-associated HCC subtypes.

A growing number of studies have employed single-cell RNA sequencing technologies to reveal cellular heterogeneity and predict cell-to-cell communications in the TIME of HCC[9] and to decipher its impact on ICB therapy response.[7,10,11] Nevertheless, single-cell RNA sequencing only measures transcriptomes of immune cells to infer their subtypes, and positional information is frequently not considered.[12] Imaging mass cytometry (IMC) is a new technology that enables spatial proteomics at the single-cell level.[13–18] The use of a high-resolution laser ablation system to transfer the tissue cell-by-cell into a time-of-flight mass cytometer allows the simultaneous quantitation of metal-tagged antibodies on formalin-fixed and paraffin-embedded (FFPE) sections,[13] thus generating a multiplexed single-cell spatial atlas. Compared with transcriptomics, IMC could accurately reflect the phenotypic and functional information of TIME.[19]

To elucidate the TIME in NASH-HCC in comparison to virus-associated HCC, here we applied IMC to construct a spatially resolved single-cell atlas from the FFPE tissue sections from patients with NASH-HCC, virus-HCC (HBV-HCC and HCV-HCC), and healthy donors. We characterized a cell-cell network in NASH-HCC leading to dysfunctional T cell immune surveillance compared to virus-associated HCC, which is mediated by immunosuppressive cells including myeloid-derived suppressor cells (MDSCs) and tumor-associated macrophages (TAMs). Together, this work unravels the complex interplay between tumor cells and immune cells constituting the TIME of NASH-HCC, and identified immune cell subsets that could be targeted for immunotherapy of NASH-HCC.

METHODS

Human sample collection

FFPE liver tissue sections from patients (16 with NASH-HCC, 6 with HBVHCC, and 5 with HCV-HCC) were collected from the First Affiliated Hospital of Sun Yat-sen University and the Sun Yat-sen University Cancer Center (Guangzhou, China). FFPE liver tissue sections of 6 healthy donors for liver transplantation were collected from Renji Hospital of Shanghai Jiaotong

University School of Medicine (Shanghai, China). All cases were confirmed by clinical history and histologically reviewed by liver pathologists. All research was conducted in accordance with both the Declarations of Helsinki and Istanbul. This study was approved by the Clinical Research Ethics Committee of the Sun Yat-sen University of Medical Science and the Shanghai Jiaotong University School of Medicine. Informed consent was obtained from all recruited patients.

Data generation from IMC

Details of FFPE tissue preparation, experiments for IMC, and image analysis pipeline are described in Supplemental Materials and Methods, http://links.lww.com/HEP/H991.

Cell type identification and composition

In order to assign each cell to a unique cell type, the clustering algorithm was used in iterative rounds with the Seurat (v4.0) in R, according to the log-transformed protein profile of signature markers. The first clustering round separated cells into 4 major cell types (ie, immune, hepatocytes, fibroblast, and endothelial). Immune cells were then clustered again to separate myeloid cells (ie, monocytic myeloid-derived suppressor cells (M-MDSCs), polymorphonuclear myeloid-derived suppressor cells (PMN-MDSCs), and TAMs). Lastly, the lymphoid cells were clustered into 7 groups (ie, $CD8^+$ T cells, $CD4^+$ T cells, regulatory T cells (T_{reg}), natural killer T cells (NKT), natural killer cells, and B cells). Immune cells with an expression profile not consistent with any of those subsets were annotated as "mix immune." Criteria used for assigning cell types can be found in Supplemental Table S3, http://links.lww.com/HEP/H992.

The relative abundance of all cell types was calculated out of total cells per section, the relative abundance of immune cell subsets for comparison of cellular composition was calculated out of total immune cells per section or per region for each section, and the relative abundance of immune cell subsets for comparison of cellular distribution across regions was calculated out of total in 1 cell type per section.

Linear discriminant analysis

Linear discriminant analysis was conducted for region classification according to cellular compositions of immune cells in each image from 16 patients with NASH-related HCC. The input data were the relative abundance of immune cell subsets calculated out of the total immune cells per image for each patient. Then, we used linear regression to depict the linear distribution of each region cluster according to data after dimension reduction.

Cellular connection analysis

The direct neighbors of each cell were identified by histoCAT using the default settings.[20] Then, we used the hypergeometric test to evaluate significantly enriched pairwise physical connections between cell types for each region from the same group of samples, as the following formula.

$$p(N_{c,n}) = \frac{\binom{N_{tn}}{N_{c,n}}\binom{N_t - N_{tn}}{N_{tc} - N_{c,n}}}{\binom{N_t}{N_{tc}}}$$

where $N_{c,n}$ is the number of links between cell c and its neighboring cell n, N_{tn} is the total number of links of cell n, N_{tc} is the total number of links of cell c, N_t is the total number of links $\sum_c N_{tc}$. The p-values <0.05 were considered as significant. The results were shown in heatmaps from R or networks from Cytoscape.

Immunoregulatory protein analysis

Positivity thresholds for Ki-67, granzyme B (GZMB), programmed cell death 1 (PD-1), programmed cell death-ligand 1 (PD-L1), and inducible T cell costimulator (ICOS) were identified according to their upper 99th percentile of the log-transformed expression data in healthy donors whereas for GZMB according to the upper 95th percentile of the log-transformed expression data in healthy donors. The relative abundance of immunoregulatory protein (IRP) coexpression patterns was calculated out of total in one cell type per region. The correlation of each pair of IRPs in each cell type was analyzed across regions for total specimens within a group using Pearson correlation analysis.

Statistics and reproducibility

For significant testing the difference in cellular compositions, we applied a 2-sided Mann-Whitney *U* test to compare proportions of cells among groups but a 2-sided Wilcoxon test for paired samples within a group. To evaluate the linear relationship between immune cells, we performed the basic function for linear regression with default parameters in R (version 4.2). The quality of the fit was evaluated and reported with *r* as measured by the Pearson correlation coefficient and *p* as measured by a 2-tailed *t* test.

RESULTS

IMC reveals a spatially resolved single-cell atlas that distinguishes HCC from healthy liver

We collected the FFPE liver tissue sections from 16 NASH-HCC, 6 HBV-HCC, 5 HCV-HCC, and 6 healthy donors (Clinical information is listed in Supplemental Table S1, http://links.lww.com/HEP/H992). The overall workflow for IMC is shown in Figure 1A. Each FFPE section was independently reviewed by 3 pathologists, and a median of 6 region of interest (ROIs) was randomly selected from tumor, margin, and peritumor (Supplemental Figure S1, http://links.lww.com/HEP/H993). IMC was performed with 35 markers, encompassing cellular markers for immune and nonimmune cell types (eg, hepatocytes, endothelial, and fibroblasts) as well as functional markers for proliferation (Ki-67) and immunoregulation (eg, GZMB, PD-1, PD-L1, and ICOS) (Supplemental Figure S2A-B, http://links.lww.com/HEP/H994 and Supplemental Table S2, http://links.lww.com/HEP/H992). In summary, biomarker and spatial information were generated for 750,405 cells from 209 ROIs.

We first classified the single cells into 13 cell types according to the expression of 23 cellular markers using Seurat clustering (Figure 1B and Supplemental Figure S2C, http://links.lww.com/HEP/H994). In a typical analysis of a ROI (Figure 1C), cellular markers in IMC images (Figure 1D) were employed to assign individual cells to hepatocytes, endothelial, fibroblast, and immune cell types (Figure 1E, left). Identified cell types were cross-validated with hematoxylin and eosin staining (Figure 1C). Infiltrating lymphocytes (Figure 1E, middle) and myeloid cells (Figure 1E, right) were further segmented into different cell subtypes according to additional immune cell markers. We thus generated a single-cell atlas for each ROI by transforming the spatial expression profiles of cellular markers (Supplemental Figure S3, http://links.lww.com/HEP/I185).

Overall, we observed significantly higher infiltration of immune cells in patients with NASH-HCC (34.5%), HBV-HCC (42.5%), and HCV-HCC (45.5%) as compared to healthy subjects (2%) (Supplemental Figure S4, http://links.lww.com/HEP/H995). Immune cell populations were also more diverse in HCC (Figure 1F), with $CD8^+$ T cells and $CD4^+$ T cells being the predominant immune cells enriched in HCC (Figure 1G). In addition, T_{reg}, NKT, MDSCs, and TAMs were uniformly induced in patients with HCC as compared to healthy subjects (Figure 1G, $p < 0.05$, 2-sided Mann-Whitney *U* test). Compared with virus-associated HCC, less $CD8^+$ T and NKT cells but more PMN-MDSCs were found in NASH-HCC $p < 0.05$, 2-sided Mann-Whitney *U* test) (Figure 1G and Supplemental Figure S4, http://links.lww.com/HEP/H995). Taken together, IMC analyses unravel marked alterations of immune cell profiles in HCC compared to healthy liver, with a more subtle difference between NASH-HCC and virus-associated HCC.

NASH-HCC demonstrates spatial heterogenicity in immune cell infiltration

To decipher the TIME in HCC, we focused on the immune cell infiltration in the different regions, including tumor, margin, and peritumor regions from patients with HCC. The margin region was further split into nontumorous (NM) and tumorous (MT) regions according to histological evaluation (Figure 2A). Linear discriminant analysis of immune cell composition demonstrated clustering of samples from the same region, but were different across regions (Figure 2B). We thus analyzed spatial dynamics of immune cell infiltration for NASH-HCC by cross-region analysis. $CD8^+$ T cells, the predominant immune cells in NASH-HCC, continuously and significantly declined from peritumor to tumor region (Figure 2C, upper; $p < 0.05$, 2-sided Wilcoxon Signed-Rank test). Consistently, the distribution of $CD8^+$ T cells dropped sharply from NM to MT (Figure 2C, lower; $p < 0.05$, 2-sided Wilcoxon Signed-Rank test). Unlike $CD8^+$ T cells, the proportion of $CD4^+$ T cells was increased in NM, but then declined in tumor (Figure 2D, lower; $p < 0.05$, 2-sided Wilcoxon Signed-Rank test), which was in agreement with a decrease of $CD4^+$ T cells in NASH-HCC.[21] We next evaluated immunosuppressive cell populations such as T_{reg} cells, MDSCs, and TAMs. T_{reg} cells showed a declining trend in the tumorous region (Figure 2E). M-MDSCs declined progressively from peritumor to tumor (Figure 2F, upper; $p < 0.05$, 2-sided Wilcoxon Signed-Rank test). Immunosuppressive cells are all preferentially distributed to the peritumorous region (Figure 2E–H; lower; $p < 0.05$, 2-sided Wilcoxon Signed-Rank test). The representative images of the spatial distribution of immune markers in different regions of NASH-HCC are shown in Figure 2I. Notably, more immune cells were distributed in the nontumorous region than in other regions in NASH-HCC, while neither HBV-HCC nor HCV-HCC showed obvious spatial heterogeneity across different regions (Supplemental Figure S5A, http://links.lww.com/HEP/H996). The downregulations of CD8+ T and NKT cells in NASH-HCC compared to virus-associated HCC were consistent across all the regions (Supplemental Figure S5B, http://links.lww.com/HEP/H996). This implied that immune cell alterations across nontumorous and tumorous regions might contribute to a unique TIME of NASH-HCC.

Immunosuppressive cells are inversely correlated with T cells in NASH-HCC

We next examined the correlation between immunosuppressive cells and T cells in the NASH-HCC TIME. $CD8^+$ T cells were negatively correlated with MDSCs

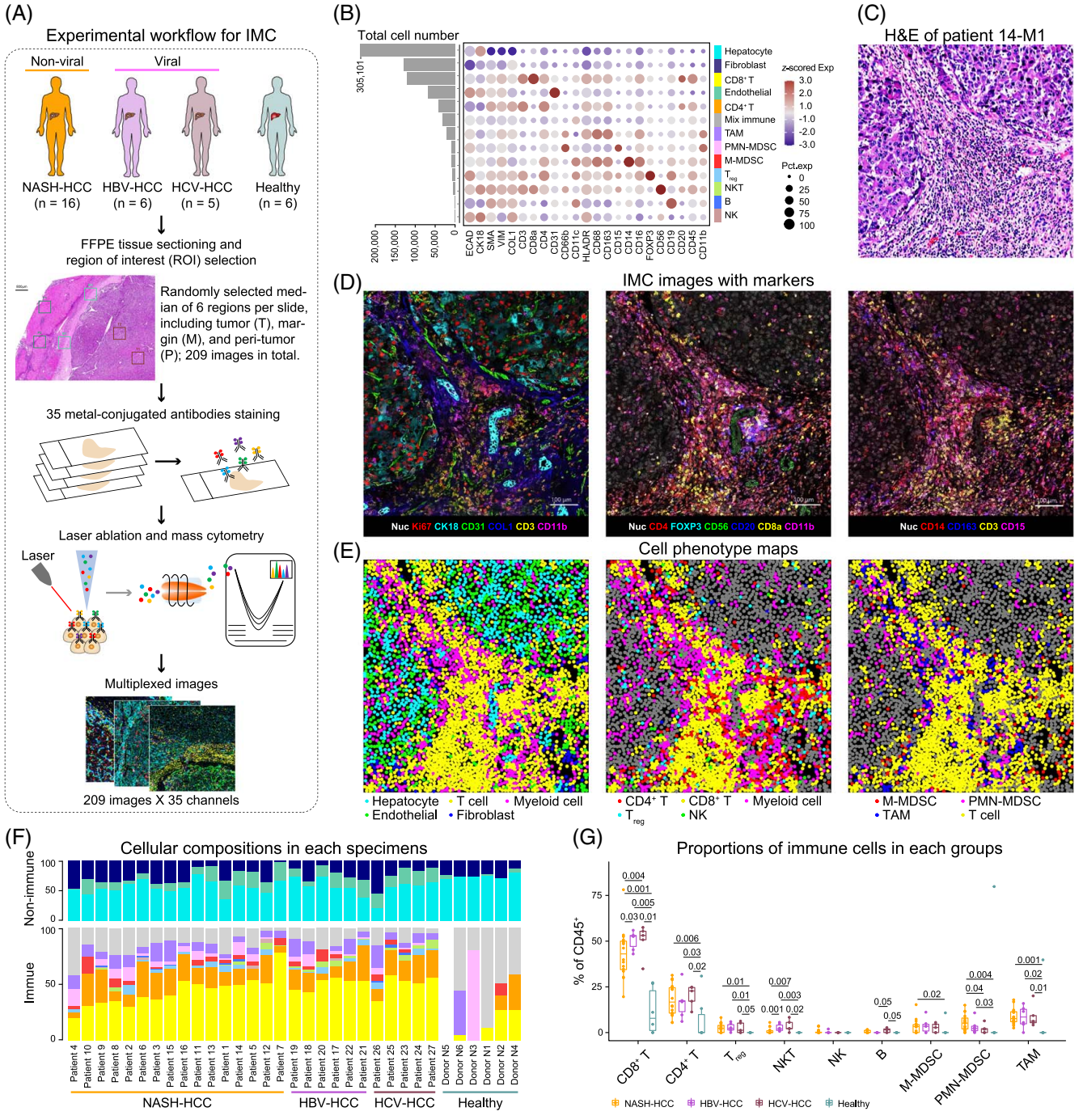

FIGURE 1 Single-cell, high-dimensional atlases of HCC histopathology. (A) Schematic diagram showing IMC workflow for acquiring highly multiplexed spatial data of liver tissue specimens from 16 patients with NASH-HCC, 11 patients with virus-associated HCC patients, and 6 healthy donors. (B) Total numbers of each cell types identified from all IMC images of liver tissues were shown in histogram, the z-scored protein expressions of each indicated markers were depicted by circle color in the bubble plot, while the percentages of each cell type expressing the corresponding markers were depicted by circle size. (C–E) H&E-stained section (C), IMC images stained with multiplexed antibody panels grouped according to cellular category (D) and corresponding cell phenotype maps (E) of representative HCC tissue specimens showing the patterns of histologic architecture, marker staining, and indicated cell types. (F) Compositions of nonimmune and immune cells in each specimen. The color panel is the same as in (B). (G) Comparisons of immune cells among groups. Each dot represented data from an individual, boxplot with whiskers and center line individually showed data from a group in the 25th–75th and the 50th percentiles, *p*-values were evaluated by 2-sided Mann-Whitney *U* test. Abbreviations: FFPE, formalin-fixed and paraffin-embedded; H&E, hematoxylin and eosin; IMC, imaging mass cytometry; M, margin; M-MDSC, monocytic myeloid-derived suppressor cell; NKT, natural killer T cell; P, peritumor; PMN-MDSC, polymorphonuclear myeloid-derived suppressor cell; ROI, region of interest; T, tumor; TAM, tumor-associated macrophage; T_{reg}, regulatory T cell.

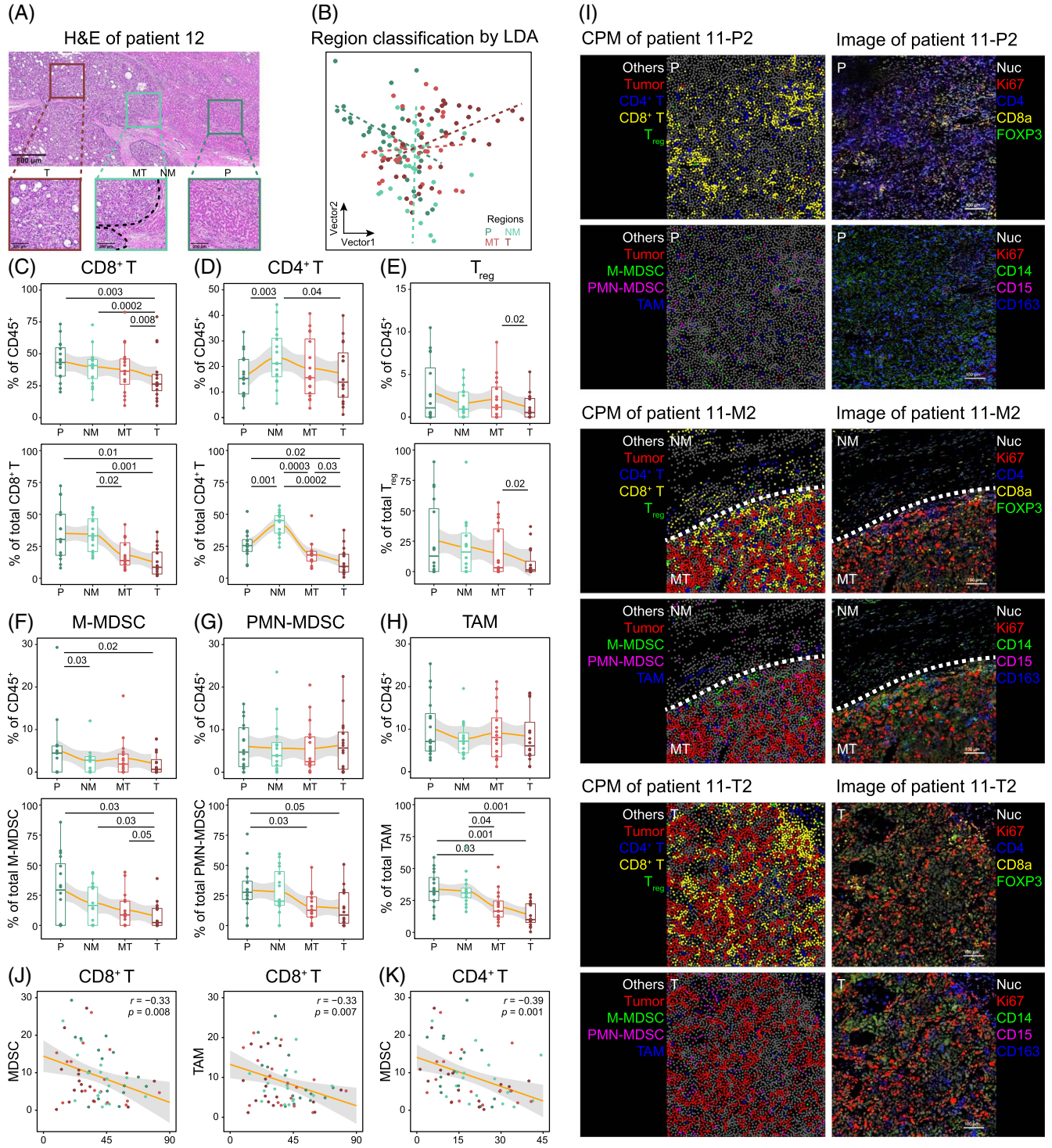

FIGURE 2 Spatial landscape of immune cells for NASH-related HCC. (A) Region classification according to pathological characteristics, including tumor (T), margin (M), and peritumor (P) regions. The dotted line depicts the tumor margin. MT belonged to the tumorous zone, while NM is in the pretumorous zone. (B) Classification of all regions from patients with NASH-HCC by LDA, according to the compositions of immune cells per region. A dotted line showed a linear distribution of each region cluster. (C–H) Spatial dynamics of proportions (on the top) and distributions (on the bottom) of immune cells. Each dot represented data from an individual, boxplot with whiskers and center line individually showed data from a group in the 25th–75th and the 50th percentiles, *p*-values were evaluated by a 2-sided Wilcoxon Signed-Rank test for paired samples. (I) Spatial distributions of immune cells shown in representative CPMs across regions (on the left) and corresponding images stained by antibodies (on the right). (J, K) Linear relationship of proportions between T and immunosuppressive cells in patients with NASH-HCC. The color of each dot represents region information, *r* represents the Pearson correlation coefficient, and *p* is the corresponding 2-sided *p*-value. Abbreviations: CPM, cell phenotype map; H&E, hematoxylin and eosin; LDA, linear discriminant analysis; M, margin; M-MDSC, monocytic myeloid-derived suppressor cell; MT, tumorous region near margin; NM, nontumorous; P, peritumor; PMN-MDSC, polymorphonuclear myeloid-derived suppressor cell; T, tumor; TAM, tumor-associated macrophage; T_{reg}, regulatory T cell.

($r = -0.33$, $p = 0.008$, Pearson correlation coefficient) and TAMs ($r = -0.33$, $p = 0.007$) (Figure 2J), while $CD4^+$ T cells were inversely correlated with MDSCs ($r = -0.39$, $p = 0.001$) (Figure 2K). In virus-associated HCC, a similar negative correlation was found between $CD8^+$ T cells and MDSCs or TAMs (Supplemental Figure S6A, http://links.lww.com/HEP/H997) as well as between $CD4^+$ T cells and M-MDSCs (Supplemental Figure S6B, http://links.lww.com/HEP/H997). Collectively, these observations supported a central role of immunosuppressive cells such as MDSCs and TAMs in inhibiting T cell infiltration in NASH-HCC.

Intratumoral immunosuppressive cells physically associate with T cells in NASH-HCC

$CD4^+$ T and $CD8^+$ T cells are crucial for antitumor immunity.[22–24] Cytotoxic $CD8^+$ T cells mediate the direct killing of cancer cells, while $CD4^+$ T helper cells activate $CD8^+$ T cells and secrete effector cytokines. Both of them are dampened by immunosuppressive cells in TIME by means of cell-cell interaction. Taking advantage of the spatial information of IMC, we evaluated the physical connectiveness between immune cells using a hypergeometric test (Supplemental Figure S7, http://links.lww.com/HEP/H998, Figure S8A, http://links.lww.com/HEP/H999, Supplemental Table S4, http://links.lww.com/HEP/H992). Focusing on the spatial dynamics of physical interactions among different immune cell types in NASH-HCC, we unraveled key connections that are altered in tumorous regions (MT, tumor) compared to nontumorous tissues (peritumor, NM) (Figure 3A). Importantly, physical connections between $CD8^+$ T cells and MDSCs that were present in tumor in NASH-HCC ($p < 0.05$, hypergeometric test) were absent in viral-associated HCC (Supplemental Figure S8B, http://links.lww.com/HEP/H999). Moreover, cell-cell connections between $CD4^+$ T and T_{reg} cells were increased in tumor for all subtypes of HCC. Consistent results were observed in individual patients across different regions (Figure 3B, Supplemental Figure S8C, http://links.lww.com/HEP/H999). Representative images from the NASH-HCC case displayed self-connection of $CD8^+$ T cells that were progressively lost from nontumorous to tumorous regions (MT, tumor) (Figure 3C), which were replaced by connection between $CD8^+$ T cells and MDSCs (Figure 3C). Similarly, the distances between $CD4^+$ T and T_{reg} cells became significantly shorter in MT and tumor compared to nontumorous regions, concomitant with the loss of self-connection among $CD4^+$ T cells (Figure 3D). In contrast, there were no differential immune cell interactions between $CD8^+$ T cells with immunosuppressive cell populations in virus-associated HCC. Collectively, these results indicate that $CD8^+$ and $CD4^+$ T cells are physically associated with intratumoral immunosuppressive cells in NASH-HCC, consistent with an impaired antitumor response.

NASH-HCC harbors immunosuppressive cells with elevated function that coincides with T cell exhaustion

Next, we sought to identify the functional states of immune cells in the TIME of NASH-HCC. We focused on 4 IRPs, GZMB, PD-1, PD-L1, and ICOS, which are considered as key molecules involved in antitumor surveillance and responsiveness to ICB therapy. We found that the expression of PD-1/PD-L1/ICOS was higher in NASH-HCC compared to virus-associated HCC, while the expression of GZMB showed an opposite trend (Supplemental Figure S9A, http://links.lww.com/HEP/H1000). When stratified according to different regions, $PD\text{-}1^+/PD\text{-}L1^+/ICOS^+$ immune cells in peritumor of NASH-HCC were significantly higher than virus-associated HCC (Supplemental Figure S9B, http://links.lww.com/HEP/H1000). Meanwhile, downregulated $GZMB^+$ immune cells in NASH-HCC occurred mainly in margin and tumor (Supplemental Figure S9B, http://links.lww.com/HEP/H1000). These results show that NASH-HCC TIME has elevated expression of checkpoint molecules, whereas cytotoxic markers were reduced, consistent with a more immunosuppressive TIME compared to virus-associated HCC.

To assign functional states to individual cell types, we analyzed the expression of these proteins in different immune cells across regions in NASH-HCC. In nontumorous regions (peritumor, NM), immune checkpoints ($PD\text{-}1^+/PD\text{-}L1^+/ICOS^+$) were predominantly expressed in T_{reg} (Figure 4A). On the other hand, PMN-MDSCs (peritumor, NM, MT) and TAMs (MT) in the boundary regions expressed PD-L1; and M-MDSCs had the highest expression of PD-L1 in tumor (Figure 4A). This indicated that major functional immunosuppressive cells shifted from T_{reg} in nontumorous tissues to MDSCs and TAMs in tumorous tissues in NASH-HCC. Notably, $CD8^+$ T cells in MT and tumor regions of NASH-HCC expressed PD-1, a T cell exhaustion marker, corroborating reports showing the unique presence of $PD\text{-}1^+CD8^+$ T cells in NASH-HCC progression.[7] Indeed, $CD8^+$ T cells in virus-associated HCC had lower expression of PD-1 compared to those in NASH-HCC, whereas PMN-MDSCs and TAMs also had lower PD-L1 expression (Supplemental Figure S9C, http://links.lww.com/HEP/H1000). For effector function (GZMB), we found that NKT had high GZMB in the tumorous regions (MT, tumor) of all HCC (Figure 4A and Supplemental Figure S9C, http://links.lww.com/HEP/H1000). Representative images displayed concordant features, including colocalization of GZMB/PD-1 with $CD8^+$ T cells, PD-1/PD-L1/ICOS with T_{reg} ($FOXP3^+$), and PD-L1 with M-MDSCs ($CD14^+$) (Figure 4B).

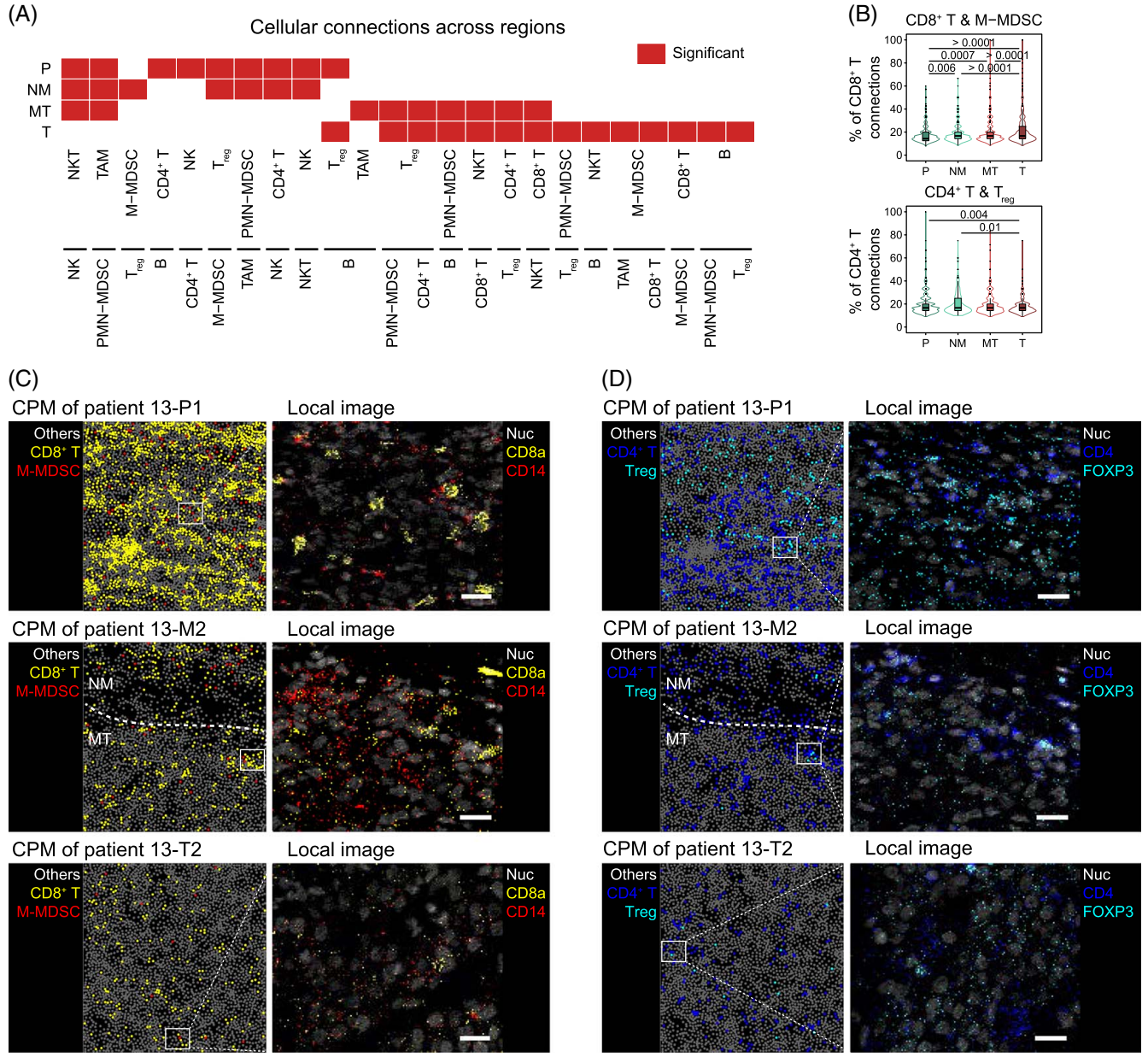

FIGURE 3 Spatial dynamics of physical connections among the different immune cell types in NASH-HCC. (A) Significant cellular connections among immune cells in different regions. (B) Proportions of $CD8^+$ T cells connecting to M-MDSCs among all connections of $CD8^+$ T cells (on the top) and proportions of $CD4^+$ T cells connecting to T_{reg} cells among all connections of $CD4^+$ T cells (on the bottom) across regions for patients with NASH-HCC. Each dot represented data from an individual, boxplot with whiskers and center line individually showed data from a group in the 25th–75th and the 50th percentiles, *p*-values were evaluated by a 2-sided Wilcoxon Signed-Rank test for paired samples. (C) Dynamic connections of $CD8^+$ T with $CD4^+$ T and PMN-MDSCs across regions are shown in representative CPMs and corresponding local images stained with antibodies. (D) Dynamic connections of $CD4^+$ T with immunosuppressive cells across regions are shown in representative CPMs and corresponding local images stained with antibodies. The bar represents 20 μm. Abbreviations: CPM, cell phenotype map; M-MDSC, monocytic myeloid-derived suppressor cell; MT, tumorous region near margin; NKT, natural killer T cell; NM, nontumorous; P, peritumor; PMN-MDSC, polymorphonuclear myeloid-derived suppressor cell; T, tumor; TAM, tumor-associated macrophage; T_{reg}, regulatory T cell.

To further elucidate specific immune cell subsets, we classified immune cells according to coexpression of functional markers (Figure 4C, D). Functional $GZMB^+CD8^+$T cells were also reduced in NASH-HCC compared to virus-associated HCC across different regions, as were $GZMB^+CD4^+$ T cells in the tumor and NM (normal margin) regions (Supplemental Figure S10, http://links.lww.com/HEP/I2). On the contrary, higher proportions of $GZMB^+CD8^+$ T cells were consistently observed in virus-associated HCC compared to NASH-HCC in all regions (Figure 4C and Supplemental Figure S10, http://links.lww.com/HEP/I2). A similar trend was found for $CD4^+$ T cells.

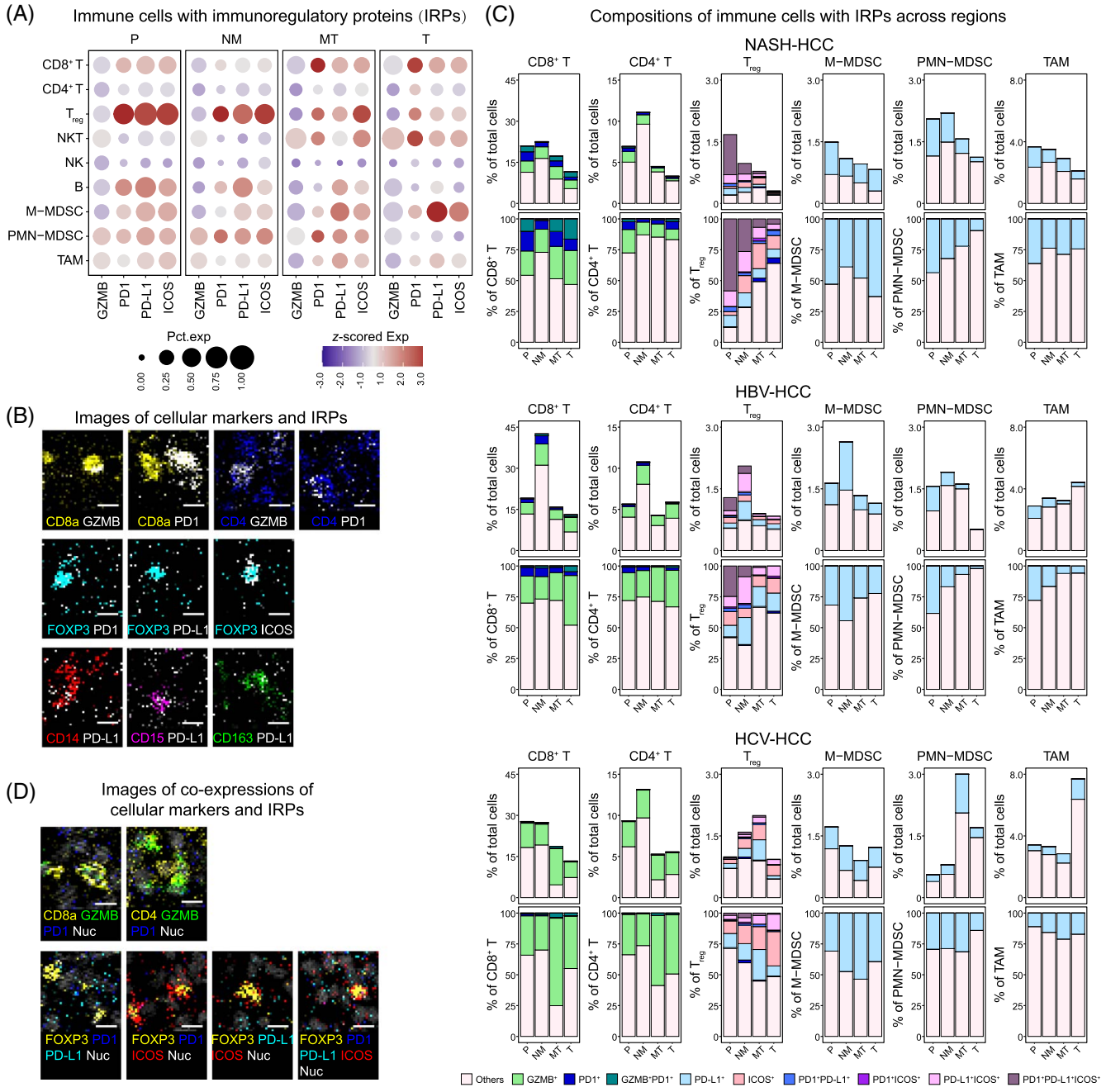

FIGURE 4 Multicellular interactions in tumor immune microenvironment of NASH-HCC. (A) Spatial dynamics of the key IRPs expressed on immune cells across different regions. Circle color in the bubble plot depicted z-scored protein expression, while circle size depicted the proportions of each cell type expressing the corresponding IRPs. (B) IRPs on immune cells validated by representative images stained with cellular markers and IRPs. The bar represents 10 μm. (C) The compositions of immune cells with IRPs across regions in NASH-HCC, HBV-HCC, and HCV-HCC. (D) Coexpression of IRPs validated by representative images. Abbreviations: GZMB, granzyme B; ICOS, inducible T cell costimulator; IRP, immunoregulatory protein; M-MDSC, monocytic myeloid-derived suppressor cell; MT, tumorous region near margin; NK, natural killer cell; NKT, natural killer T cell; NM, nontumorous; P, peritumor; PD-1, programmed cell death 1; PD-L1, programmed cell death-ligand 1; PMN-MDSC, polymorphonuclear myeloid-derived suppressor cell; T, tumor; TAM, tumor-associated macrophage; T_{reg}, regulatory T cell.

Among immunosuppressive cells, PD-1$^+$PD-L1$^+$ICOS$^+$ T_{reg} was abundant in peritumor and NM regions of NASH-HCC compared to virus-associated HCC (Figure 4C and Supplemental Figure S10, http://links.lww.com/HEP/I2). Meanwhile, PD-L1$^+$ M-MDSC was still highly enriched in the tumorous region of NASH-HCC (Figure 4C). Accordingly, we observed reciprocal association of PD-1$^+$PD-L1$^+$ICOS$^+$ T_{reg} with PD-L1$^+$ M-MDSCs and PD-L1$^+$ TAMs across regions in NASH-HCC. These observations suggested the shift of immunosuppressive cells from T_{reg} to MDSCs from nontumorous to tumorous regions in NASH-HCC (Figure 4A). Importantly, PD-1$^+$ T cells positively correlated with PD-L1$^+$ MDSCs across regions in all

HCCs, implying corroboration between exhausted T cells and MDSCs. The apparent lack of T cell exhaustion in virus-associated HCC underlies its sensitivity to ICB therapy[25] compared to NASH-HCC. Taken together, immunosuppression in NASH-HCC was reflected by the accumulation of PD-L1$^+$ MDSCs and exhausted PD-1$^+$CD8$^+$ T cells in tumorous tissues.

Integrated spatial and functional analysis implies direct interplay between immune cells to foster an immunosuppressive TIME in NASH-HCC

We next dissected the interplay among immune cell populations by integrating spatial (Figure 3) and functional information (Figure 5). Overall, a more complex network of CD8$^+$ T cells (Figure 5A) and CD4$^+$ T cells (Figure 5B) with other immune cells was observed in peritumor compared to margin and tumorous regions in all HCCs, reflecting a higher diversity of immune cells in the normal region. In NASH-HCC, PD-1$^+$CD8$^+$ T cells neighbored with PD-1$^+$ M-MDSCs, PD-1$^+$ PMN-MDSCs, PD-1$^+$CD4$^+$ T cells in all regions; while GZMB$^+$CD8$^+$ T cells neighbored CD4$^+$ T cells, T_{reg}, M-MDSCs (especially PD-1$^+$ M-MDSCs) and PMN-MDSCs in all regions, PD-1$^+$PD-L1$^+$ICOS$^+$/PD-L1$^+$ICOS$^+$ T_{reg} in nontumorous regions but PD-L1$^+$ M-MDSCs and PD-L1$^+$ TAMs in tumorous regions (Figure 5A and Supplemental Figure S11, http://links.lww.com/HEP/I3). These observations might explain immunosuppression of cytotoxic CD8$^+$ T in NASH-HCC from the perspective of cell-cell cross talk. For CD4$^+$ T cells, its connections with other immune cells were similar to CD8$^+$ T cells (Figure 5B and Supplemental Figure S11, http://links.lww.com/HEP/I3), which implied a similar mechanism for suppression of CD4$^+$ T cells in NASH-HCC.

Compared to NASH-related HCC, interactions of CD8$^+$ T and CD4$^+$ T cells with other immune cells were less complicated in virus-associated HCC, particularly for PD-1$^+$CD8$^+$ T cells (Figure 5 and Supplemental Figure S11, http://links.lww.com/HEP/I3). In tumorous regions, GZMB$^+$CD8$^+$ T cells were connected with GZMB$^+$CD4$^+$ T cells, PD-L1$^+$/ICOS$^+$/PD-L1$^+$ICOS$^+$ T_{reg}, PD-L1$^+$ M-MDSCs, and PD-L1$^+$ TAMs in HCV-related HCC, whereas in HBV-related HCC they were connected with other immune cells with IRPs, but not PMN-MDSCs (Figure 5A and Supplemental Figure S11, http://links.lww.com/HEP/I3). Connections of PD-1$^+$CD8$^+$ T cells with immunosuppressive cells were largely absent in tumorous regions of virus-associated HCC (Figure 5A). Neighboring connections between PD-1$^+$CD8$^+$ T cells with immunosuppressive PMN-MDSCs, M-MDSCs, and TAMs were highly enriched in NASH-HCC compared to virus-associated HCC (Supplemental Figure S11, http://links.lww.com/HEP/I3). Multicolor fluorescent staining was performed to analyze connections between PD-1$^+$CD8$^+$ T cells and PD-L1$^+$ MDSCs and TAMs in tumorous regions of NASH-HCC and virus-associated HCC. We found that exhausted PD-1$^+$CD8$^+$ T cells connected with PD-L1$^+$ MDSCs and TAMs in NASH-HCC but not viral HCC (Supplemental Figure S12, http://links.lww.com/HEP/I4). Immunoregulatory connections of CD4$^+$ T cells with other immune cells were similar to that of CD8$^+$ T cells in virus-associated HCC (Figure 5B). Together, the immunosuppressive TIME in NASH-HCC was dominated by interactions of PD-1$^+$CD8$^+$ T cells with immunosuppressive cells, which were diminished in virus-associated HCC.

Immune cells, but not HCC cells, foster an immunosuppressive TIME in NASH-HCC

We finally explored the potential interactions between HCC cells and immune cells in NASH-HCC. Immune checkpoints, such as PD-L1, have been reported to be expressed in HCC cells and mediate immune evasion.[26] As shown in Figure 6A, PD-1, PD-L1, and ICOS were predominantly expressed in immune cells in both the nontumorous and tumorous tissues of NASH-HCC ($p < 0.05$, 2-sided Wilcoxon test for paired samples). This was in contrast with virus-associated HCC, where no significant difference was found in PD-1, PD-L1, and ICOS expression between immune cells, HCC, and hepatocytes (Figure 6A). Overall, expressions of PD-1, PD-L1, and ICOS were low in tumor cells, and no difference was found between NASH-associated or virus-associated HCC (Figure 6B). In NASH-HCC, quantitative evaluation showed that the proportion of PD-L1$^+$ cells declined in HCC cells compared to hepatocytes (Figure 6C). Coexpression of immune checkpoints, evident in hepatocytes, was absent in HCC cells (Figure 6C). Representative images from nontumorous and tumorous regions verified that PD-L1 expression in HCC was lower than that in hepatocytes in NASH-HCC (Figure 6D). This implies that immunosuppression in TIME of NASH-HCC was primarily mediated by infiltrating immune cells, such as MDSCs and TAMs, but not HCC cells.

Consistent with this notion, network analysis demonstrated that HCC cells (MT, tumor) had fewer connections with immune cells with positive IRPs compared to hepatocytes (peritumor, NM) for all HCCs (Figure 6E). Although the majority of HCC cells was devoid of immune checkpoints, they nevertheless maintained stronger connections to M-MDSCs, PMN-MDSCs, and TAMs in NASH-HCC as compared to virus-associated HCC, which could antagonize the cytotoxic effect of effector T cells (Figure 6E). In contrast, connections between HCC cells and GZMB$^+$ CD8$^+$ T cells and GZMB$^+$ NKT cells were largely abolished in virus-associated HCCs (Figure 6E). These

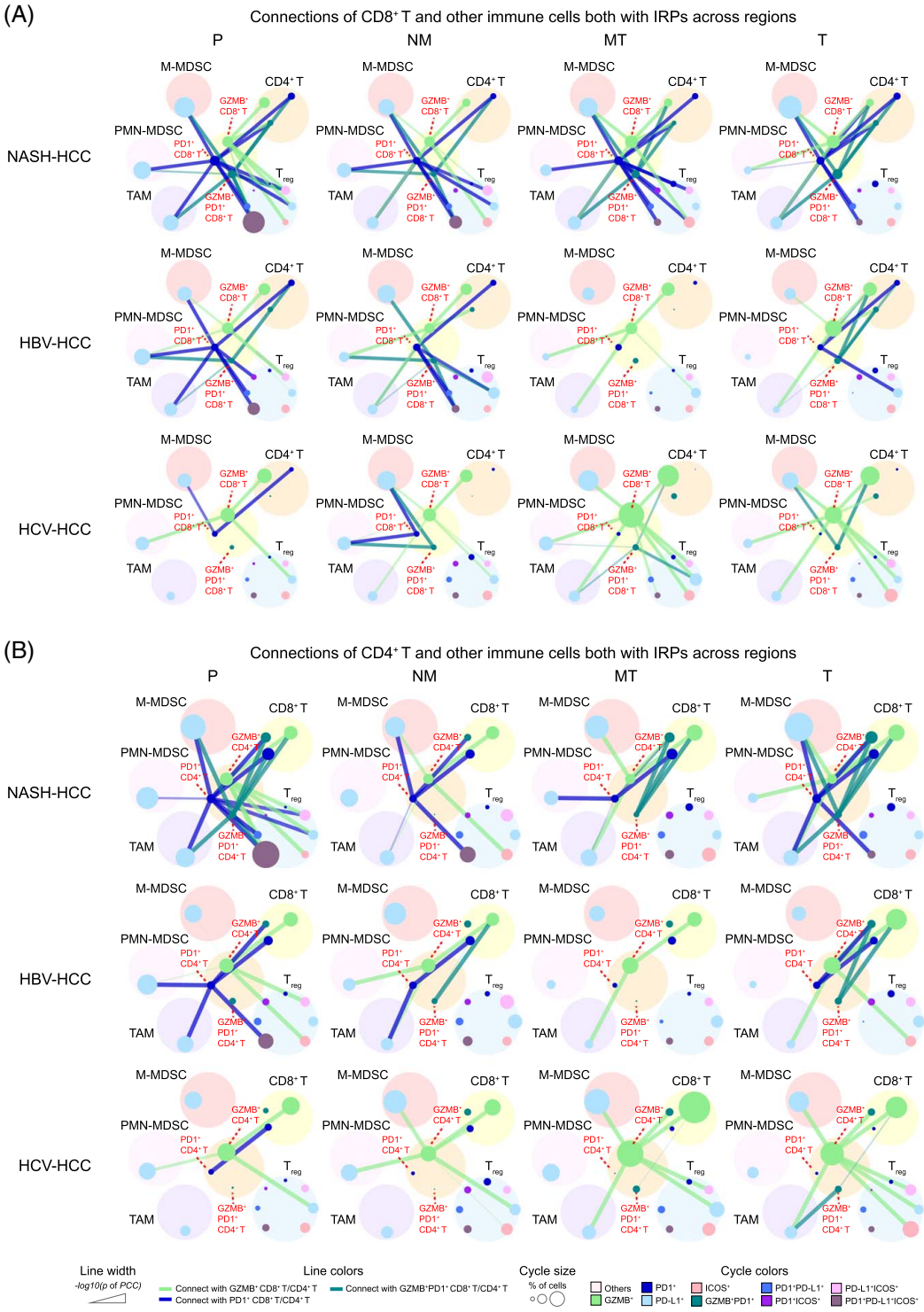

FIGURE 5 Spatial dynamics of interplay between different subsets of CD8$^+$ T and CD4$^+$ T cells and immunosuppressive immune cells defined by their IRPs. (A) Physical connections between CD8$^+$ T cells and other immune cells expressing IRPs across regions. (B) Physical connections between CD4$^+$ T cells and other immune cells expressing IRPs across regions. Abbreviations: GZMB, granzyme B; ICOS, inducible T cell costimulator; IRP, immunoregulatory protein; M-MDSC, monocytic myeloid-derived suppressor cell; MT, tumorous region near margin; NKT, natural killer T cell; NM, nontumorous; P, peritumor; PCC, Pearson correlation coefficient; PD-1, programmed cell death 1; PD-L1, programmed cell death-ligand 1; PMN-MDSC, polymorphonuclear myeloid-derived suppressor cell; T, tumor; TAM, tumor-associated macrophage; T_{reg}, regulatory T cell.

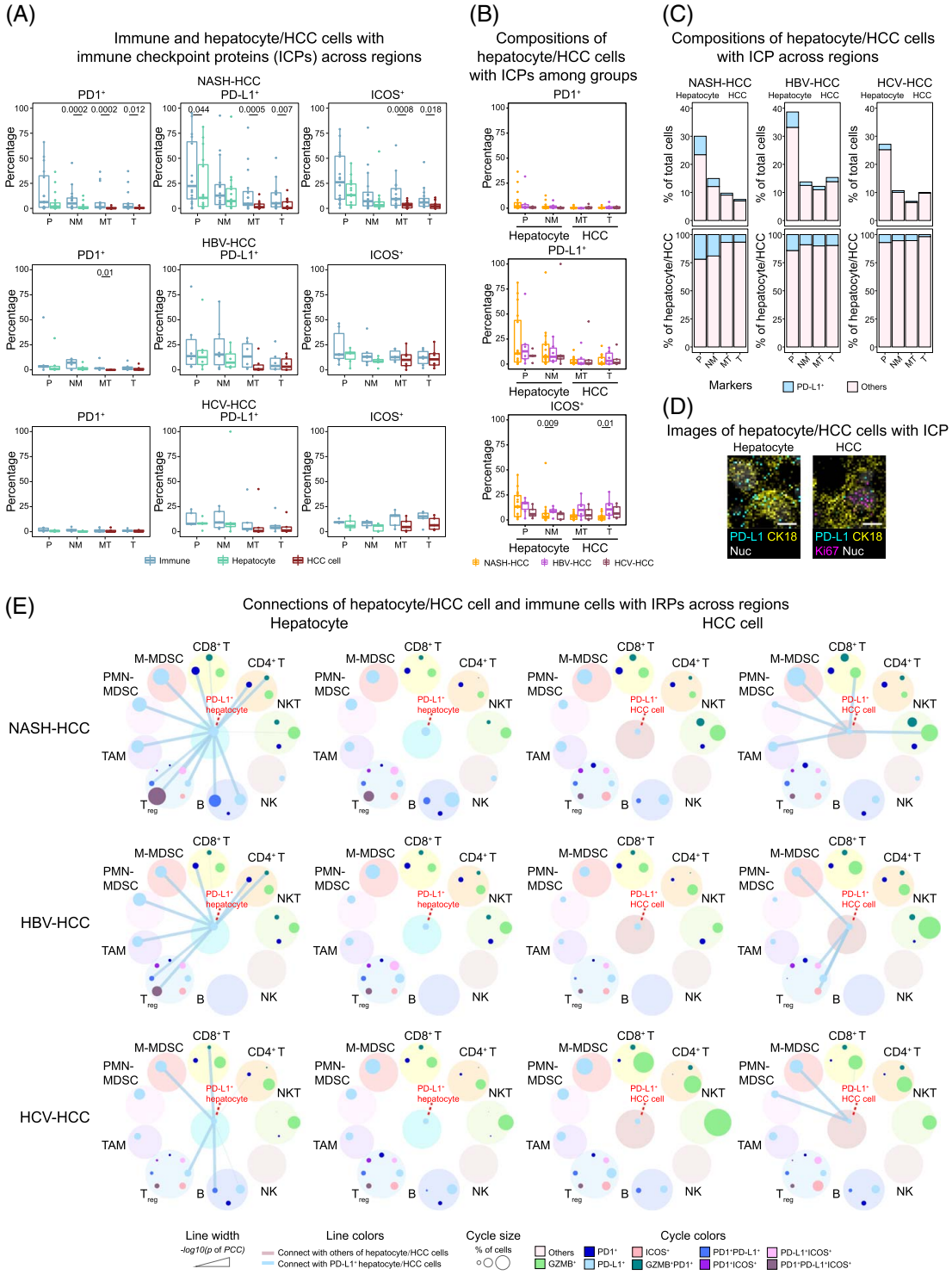

FIGURE 6 Spatial dynamics of interplay between hepatocyte/HCC cells and immune cells in different functional states. (A) Percentage of immune and hepatocyte/HCC cells expressing ICPs across regions. Each dot represented data from a patient, boxplot with whiskers and center line individually showed data from a group in the 25th–75th and the 50th percentiles, *p*-values were evaluated by 2-sided Wilcoxon test for paired samples. (B) Proportion of hepatocyte/HCC cells expressing ICPs across regions among different HCC groups. Each dot represented data from an individual, boxplot with whiskers and center line individually showed data from a group in the 25th–75th and the 50th percentiles, *p*-values were evaluated by a 2-sided Mann-Whitney *U* test. (C) Compositions of hepatocyte/HCC cells with ICPs across regions. (D) ICPs on hepatocyte/HCC cells were validated by representative images stained with cellular markers and ICPs. The bar represents 10 μm. (E) Dynamic connections between hepatocyte/HCC cells and immune cells with IRPs across regions. Abbreviations: GZMB, granzyme B; ICOS, inducible T cell costimulator; ICP, immune checkpoint proteins; IRP, immunoregulatory protein; M, margin; M-MDSC, monocytic myeloid-derived suppressor cell; MT, tumorous region near margin; NKT, natural killer T cell; NM, nontumorous; P, peritumor; PD-1, programmed cell death 1; PD-L1, programmed cell death-ligand 1; PMN-MDSC, polymorphonuclear myeloid-derived suppressor cell; T, tumor; TAM, tumor-associated macrophage; T_{reg}, regulatory T cell.

observations suggest that the immunosuppressive TIME in NASH-HCC was maintained by MDSCs and TAMs residing in close proximity with HCC cells, thus conferring protection against effector T cells.

DISCUSSION

NASH-HCC harbors a unique TIME that drives poor survival and nonresponse to ICB therapy. Although single-cell sequencing has demonstrated distinctive immune cell subsets in NASH-HCC[7] in comparison to virus-associated HCC, spatial organization, and cell-cell connections among tumor cells, immune cells, and stromal cells remain largely unknown. Here, we deciphered the complex TIME of NASH-HCC in comparison to virus-associated HCC by generating highly multiplexed single-cell spatial atlases using IMC of clinical FFPE specimens. Based on 35 biomarkers, over 750,000 individual cells were categorized into 13 distinct cell types, together with the expression of key immune functional markers. Our work offers for the first time a roadmap integrating the spatial, phenotypical, and functional information of the TIME in NASH-HCC and highlights potential mechanisms causing the failure of ICB therapy in NASH-HCC.

We discovered a major increase in immune cell infiltration in HCC samples compared to healthy livers, particularly immunosuppressive MDSCs and TAMs, in keeping with the fact that these cells were frequently enriched in cancers[27,28] and their protumorigenic potential.[29] Next, spatial analysis revealed that immune cells were not evenly distributed across the adjacent normal, margin, and intratumoral regions. Immune cells abundance was the highest in adjacent nontumorous tissues and largely declined closer to tumors. Hence, immunologically "hot" adjacent and margin regions might overshadow an intratumoral immune desert with nonspatial approaches. In addition, substantial heterogeneity exists in immune cell abundance, phenotypes, and function across different regions. Our findings underlie that spatial information is essential to ensure a more comprehensive understanding of TIME in NASH-HCC.

We further delineated cell-cell interactions among immune cells in NASH-HCC based on their proximity in IMC scans. Most notably, the connections between $CD4^+$ T cells and $CD8^+$ T cells in the tumors of NASH-HCC were replaced by extensive interactions with immunosuppressive cells, including MDSCs and TAMs. MDSCs promote T cell tolerance in cancers by expressing arginase 1 (ARG1) and inducible nitric oxide synthase,[6,7] which deplete arginine in the TIME to impair T cell effector function, whereas TAMs secrete TGF-β to suppress effector T cell function and promote T_{reg} differentiation.[29] These antagonistic interactions might impede effective antitumor immunity in NASH-HCC.

In light of the intrinsic resistance of NASH-HCC to ICB therapy, we next determined the expression of markers of effector (GZMB) and exhaustion (PD-1) status, as well as immune inhibitory checkpoints (PD-L1, ICOS). Significant heterogeneity was observed in different regions of NASH-HCC. T_{reg} and M-MDSCs are predominant cells expressing the immune checkpoints (PD-L1, ICOS) in the nontumorous and tumorous regions, respectively, implying distinct mechanisms in eliciting T cell tolerance in a region-dependent manner. Supporting this notion, T_{reg} cells are normally resident in the hepatic microenvironment to limit excessive immune response.[30] MDSCs, on the other hand, are pathologically activated in tumors.[31] Given the proximity of PD-$L1^+$ MDSCs with effector T cells in NASH-HCC, it is unsurprising to observe T cells dysfunction in the tumors of NASH-HCC. Correspondingly, we observed a significant increase in PD-1 exhaustion marker in both $CD8^+$ T and $CD4^+$ T cells. Integrated spatial and functional analysis further showed that PD-1^+CD8^+ T and PD-1^+CD4^+ T cells connected with T_{reg} cells, M-MDSCs, and TAMs in NASH-HCC. Network analyses validated more extensive interactions between $CD4^+$ and $CD8^+$ T cells with immunosuppressive cells in NASH-HCC as compared to virus-associated HCC. These observations not only supported reports on the enrichment of exhausted PD-1^+CD8^+ T cells within tumor of NASH-related HCC,[7] but also provided a hypothesis that T cell exhaustion in the NASH-HCC TIME involved cell-cell cross talk between T cells with MDSCs and TAMs.

Tumor intrinsic factors, such as mutational load[32,33] and PD-L1 expression[34] modulate antitumor immunity and are predictive biomarkers for response toward ICB therapy. We thus explored the interplay between HCC cells and immune cells in NASH-HCC. NASH-HCC tumor cells have downregulated immune checkpoints as compared to normal hepatocytes in adjacent nontumorous regions, which is consistent with previous reports and suggests that tumor cells do not confer a direct immunosuppressive effect. As a consequence, it is the immune cells, but not tumor cells, that primarily express immune checkpoints in the NASH-HCC TIME. While hepatocytes showed extensive networks with infiltrating immune cells, NASH-HCC tumor cells had reduced connections with immune cells, only maintaining essential interactions with MDSCs and TAMs. The lack of connections between NASH-HCC tumor cells with T cells lend us to reason that MDSCs and TAMs are responsible expressing immune checkpoints for eliciting T cell exhaustion in NASH-HCC. In agreement with this, PD-L1 has been shown to be expressed on MDSCs[35] and TAMs[36] in tumors. Attenuated interaction with immune cells, especially T cells and natural killer cells, also reflect successful immune evasion by tumor cells. Collectively, our data suggest that targeting of immunosuppressive cells, such as MDSCs and TAMs, are potential strategies for overcoming ICB resistance in

NASH-HCC. Indeed, recent work has reported that targeting of CXCR2, a receptor for MDSCs, is effective in sensitizing NASH-HCC to anti-PD-1 therapy.[37] Our work, therefore, suggests targeting of immunosuppressive immune cells in TIME might improve ICB therapy efficacy in NASH-HCC.

In conclusion, our work provides the first detailed spatial map of single-cell phenotypes and multicellular connections in NASH-HCC. We demonstrate that MDSCs and TAMs as major culprits in promoting T cell exhaustion and immune evasion in NASH-HCC, which provides a basis for future strategies to overcome ICB resistance in NASH-HCC.

AUTHOR CONTRIBUTIONS

Jun Yu designed, supervised the study, and revised the manuscript; Xiaoxing Li collected clinical samples and supervised the study; Lina Wang and Liang Cong generated the raw data and performed experiments; Meiyi Li performed data analyses and drafted the manuscript; Chi Chun Wong drafted the manuscript; Xiang Zhang and Huarong Chen commented on the study; Tao Zeng and Bin Li assisted in the cell segmentation and data analysis; Xian Jia helped with the IMC staining; Jihui Huo and Xiaoxue Ren helped with the multiplex immunofluorescence staining; Yuhua Huang assisted in the pathological analysis; Sui Peng and Ming Kuang provided human samples, Joseph JY Sung, Lixia Xu and Guo Fu commented on the study.

FUNDING INFORMATION

This work was supported by Funding support from the First Affiliated Hospital, Sun Yat-sen University to Institute of Precision Medicine, Guangzhou, China; Hong Kong ITC to State Key Laboratory of Digestive Disease (8420106); Guangdong Basic and Applied Basic Research Fund (2022B1515120031).

CONFLICTS OF INTEREST

The authors have no conflicts to report.

ORCID

Chi Chun Wong https://orcid.org/0000–0003–1362–3541

Jun Yu https://orcid.org/0000–0001–5008–2153

REFERENCES

1. Sung H, Ferlay J, Siegel RL, Laversanne M, Soerjomataram I, Jemal A, et al. Global Cancer Statistics 2020: GLOBOCAN estimates of incidence and mortality worldwide for 36 cancers in 185 countries. CA Cancer J Clin. 2021;71:209–49.
2. Wong VW, Chitturi S, Wong GL, Yu J, Chan HL, Farrell GC. Pathogenesis and novel treatment options for non-alcoholic steatohepatitis. Lancet Gastroenterol Hepatol. 2016;1:56–67.
3. Yu J, Shen J, Sun TT, Zhang X, Wong N. Obesity, insulin resistance, NASH and hepatocellular carcinoma. Semin Cancer Biol. 2013;23:483–91.
4. Xu W, Zhang X, Wu JL, Fu L, Liu K, Liu D, et al. O-GlcNAc transferase promotes fatty liver-associated liver cancer through inducing palmitic acid and activating endoplasmic reticulum stress. J Hepatol. 2017;67:310–20.
5. Liu D, Wong CC, Fu L, Chen H, Zhao L, Li C, et al. Squalene epoxidase drives NAFLD-induced hepatocellular carcinoma and is a pharmaceutical target. Sci Transl Med. 2018;10:eaap9840.
6. Dudek M, Pfister D, Donakonda S, Filpe P, Schneider A, Laschinger M, et al. Auto-aggressive CXCR6(+) CD8 T cells cause liver immune pathology in NASH. Nature. 2021;592:444–9.
7. Pfister D, Nunez NG, Pinyol R, Govaere O, Pinter M, Szydlowska M, et al. NASH limits anti-tumour surveillance in immunotherapy-treated HCC. Nature. 2021;592:450–6.
8. Cheng AL, Qin S, Ikeda M, Galle PR, Ducreux M, Kim TY, et al. Updated efficacy and safety data from IMbrave150: atezolizumab plus bevacizumab vs. sorafenib for unresectable hepatocellular carcinoma. J Hepatol. 2022;76:862–73.
9. Ringelhan M, Pfister D, O'Connor T, Pikarsky E, Heikenwalder M. The immunology of hepatocellular carcinoma. Nat Immunol. 2018;19:222–32.
10. Llovet JM, Castet F, Heikenwalder M, Maini MK, Mazzaferro V, Pinato DJ, et al. Immunotherapies for hepatocellular carcinoma. Nat Rev Clin Oncol. 2022;19:151–72.
11. Mi H, Ho WJ, Yarchoan M, Popel AS. Multi-scale spatial analysis of the tumor microenvironment reveals features of cabozantinib and nivolumab efficacy in hepatocellular carcinoma. Front Immunol. 2022;13:892250.
12. Weber C. Single-cell spatial transcriptomics. Nat Cell Biol. 2021;23:1108.
13. Giesen C, Wang HA, Schapiro D, Zivanovic N, Jacobs A, Hattendorf B, et al. Highly multiplexed imaging of tumor tissues with subcellular resolution by mass cytometry. Nat Methods. 2014;11:417–22.
14. Keren L, Bosse M, Marquez D, Angoshtari R, Jain S, Varma S, et al. A structured tumor-immune microenvironment in triple negative breast cancer revealed by multiplexed ion beam imaging. Cell. 2018;174:1373–387. e1319.
15. Black S, Phillips D, Hickey JW, Kennedy-Darling J, Venkataraaman VG, Samusik N, et al. CODEX multiplexed tissue imaging with DNA-conjugated antibodies. Nat Protoc. 2021;16:3802–5.
16. Jackson HW, Fischer JR, Zanotelli VRT, Ali HR, Mechera R, Soysal SD, et al. The single-cell pathology landscape of breast cancer. Nature. 2020;578:615–20.
17. Schurch CM, Bhate SS, Barlow GL, Phillips DJ, Noti L, Zlobec I, et al. Coordinated cellular neighborhoods orchestrate antitumoral immunity at the colorectal cancer invasive front. Cell. 2020;183:838.
18. McCaffrey EF, Donato M, Keren L, Chen Z, Delmastro A, Fitzpatrick MB, et al. The immunoregulatory landscape of human tuberculosis granulomas. Nat Immunol. 2022;23:318–29.
19. Mund A, Coscia F, Kriston A, Hollandi R, Kovacs F, Brunner AD, et al. Deep visual proteomics defines single-cell identity and heterogeneity. Nat Biotechnol. 2022;40:1231–40.
20. Schapiro D, Jackson HW, Raghuraman S, Fischer JR, Zanotelli VRT, Schulz D, et al. histoCAT: Analysis of cell phenotypes and interactions in multiplex image cytometry data. Nat Methods. 2017;14:873–6.
21. Ma C, Kesarwala AH, Eggert T, Medina-Echeverz J, Kleiner DE, Jin P, et al. NAFLD causes selective CD4(+) T lymphocyte loss and promotes hepatocarcinogenesis. Nature. 2016;531:253–7.
22. Mempel TR, Pittet MJ, Khazaie K, Weninger W, Weissleder R, von Boehmer H, et al. Regulatory T cells reversibly suppress cytotoxic T cell function independent of effector differentiation. Immunity. 2006;25:129–41.
23. Halle S, Halle O, Forster R. Mechanisms and dynamics of T cell-mediated cytotoxicity in vivo. Trends Immunol. 2017;38:432–43.

24. Zhang N, Bevan MJ. CD8(+) T cells: Foot soldiers of the immune system. Immunity. 2011;35:161–8.
25. Yau T, Kang YK, Kim TY, El-Khoueiry AB, Santoro A, Sangro B, et al. Efficacy and safety of nivolumab plus ipilimumab in patients with advanced hepatocellular carcinoma previously treated with sorafenib: The CheckMate 040 Randomized Clinical Trial. JAMA Oncol. 2020;6:e204564.
26. Juneja VR, McGuire KA, Manguso RT, LaFleur MW, Collins N, Haining WN, et al. PD-L1 on tumor cells is sufficient for immune evasion in immunogenic tumors and inhibits CD8 T cell cytotoxicity. J Exp Med. 2017;214:895–904.
27. Kumar V, Patel S, Tcyganov E, Gabrilovich DI. The nature of myeloid-derived suppressor cells in the tumor microenvironment. Trends Immunol. 2016;37:208–20.
28. Wan S, Zhao E, Kryczek I, Vatan L, Sadovskaya A, Ludema G, et al. Tumor-associated macrophages produce interleukin 6 and signal via STAT3 to promote expansion of human hepatocellular carcinoma stem cells. Gastroenterology. 2014; 147:1393–404.
29. Song G, Shi M, Zhang M, Goswami S, Afridi S, Meng L, Ma J, et al. Global immune characterization of HBV/HCV-related hepatocellular carcinoma identifies macrophage and T-cell subsets associated with disease progression. Cell Discov. 2020;6:90.
30. Denning TL, Wang YC, Patel SR, Williams IR, Pulendran B. Lamina propria macrophages and dendritic cells differentially induce regulatory and interleukin 17-producing T cell responses. Nat Immunol. 2007;8:1086–94.
31. Wawman RE, Bartlett H, Oo YH. Regulatory T cell metabolism in the hepatic microenvironment. Front Immunol. 2017;8:1889.
32. Bronte V, Brandau S, Chen SH, Colombo MP, Frey AB, Greten TF, et al. Recommendations for myeloid-derived suppressor cell nomenclature and characterization standards. Nat Commun. 2016; 7:12150.
33. Litchfield K, Reading JL, Puttick C, Thakkar K, Abbosh C, Bentham R, et al. Meta-analysis of tumor- and T cell-intrinsic mechanisms of sensitization to checkpoint inhibition. Cell. 2021; 184:596–614. e514.
34. Jardim DL, Goodman A, de Melo Gagliato D, Kurzrock R. The challenges of tumor mutational burden as an immunotherapy biomarker. Cancer Cell. 2021;39:154–73.
35. Davis AA, Patel VG. The role of PD-L1 expression as a predictive biomarker: An analysis of all US Food and Drug Administration (FDA) approvals of immune checkpoint inhibitors. J Immunother Cancer. 2019;7:278.
36. Noman MZ, Desantis G, Janji B, Hasmim M, Karray S, Dessen P, et al. PD-L1 is a novel direct target of HIF-1alpha, and its blockade under hypoxia enhanced MDSC-mediated T cell activation. J Exp Med. 2014;211:781–90.
37. Petty AJ, Dai R, Lapalombella R, Baiocchi RA, Benson DM, Li Z, et al. Hedgehog-induced PD-L1 on tumor-associated macrophages is critical for suppression of tumor-infiltrating CD8+ T cell function. JCI Insight. 2021;6:e146707.
38. Leslie J, Mackey JBG, Jamieson T, Ramon-Gil E, Drake TM, Fercoq F, et al. CXCR2 inhibition enables NASH-HCC immunotherapy. Gut. 2022.;71:2093–106.

How to cite this article: Li M, Wang L, Cong L, Wong CC, Zhang X, Chen H, et al. Spatial proteomics of immune microenvironment in nonalcoholic steatohepatitis-associated hepatocellular carcinoma. Hepatology. 2024;79:560–574. https://doi.org/10.1097/HEP.0000000000000591